



Spatial aerosol deposition correlated to anatomic feature development in 6-year-old upper airway computational models

Emily L. Kolewe^a, Saurav Padhye^a, Ian R. Woodward^a, Jinyong Wee^b, Tariq Rahman^b, Yu Feng^c, Jenna W. Briddell^d, Catherine A. Fromen^{a,*}

^a Department of Chemical and Biomolecular Engineering, University of Delaware, Newark, DE, USA

^b Department of Biomedical Research, Nemours Children's Hospital, Wilmington, DE, USA

^c Department of Chemical Engineering, Oklahoma State University, Stillwater, OK, USA

^d Division of Otorhinolaryngology, Department of Surgery, Nemours Children's Hospital, Wilmington, DE, USA

ARTICLE INFO

Keywords:

Pediatric
Development
Airway
Anatomy
CFPD

ABSTRACT

The upper airways of children undergo developmental changes around age 6, yielding differences between adult and pediatric anatomies. These differences include the cricoid ring area shape, the location of narrowest constriction, and the angle of the epiglottis, all of which are expected to alter local fluid dynamic profiles and subsequent upper airway deposition and downstream aerosol delivery of inhaled therapeutics. In this work, we quantify “pediatric”-like and “adult”-like geometric and fluid dynamic features of two computed tomography (CT)-scan derived models of 6-year-old upper airways in healthy subjects and compare to an idealized model. The two CT-scan models had a mixture of “adult”- and “pediatric”-like anatomic features, with Subject B exhibiting more “pediatric”-like features than Subject A, while the idealized model exhibited entirely “adult”-like features. By computational fluid-particle dynamics, these differences in anatomical features yielded distinct local fluid profiles with altered aerosol deposition between models. Notably, the idealized model better predicted deposition characteristics of Subject A, the more “adult”-like model, including the relationship between the impaction parameter, $d_p^2 Q$ and the fraction of deposition across a range of flow rates and particle diameters, as well as deposition of an approximate pharmaceutical particle size distribution model. Our results with even this limited dataset suggest that there are key personalized metrics that are influenced by anatomical development, which should be considered when developing pediatric inhalable therapeutics. Quantifying anatomical development and correlating to aerosol deposition has the potential for high-throughput developmental characterization and informing desired aerosol characteristics for pediatric applications.

1. Introduction

Human upper airways consist of the naso-oropharynx, supraglottis, glottis, subglottis, and trachea and are comprised of, and influenced by, anatomical features such as the epiglottis and cricoid ring [1]. As can be seen in Fig. 1, pediatric upper airways undergo major changes prior to adulthood; while the overall anatomic features increase in size through development, the larynx sits higher and more anterior in pediatric subjects before transitioning lower in the neck in adult subjects, and the cricoid ring is funnel-shaped in pediatric subjects before transitioning to cylindrical in adults [2–5]. Furthermore, the narrowest anatomical feature of the pediatric throat differs from that of an adult, where the glottis represents the most significant constriction. In the pediatric

airway the narrowest portion is more dynamic [4]. The vocal folds of the glottis move during respiration and speech and are capable of narrowing (adducting) past the diameter of any other anatomical feature; however, on dilation (abduction), the glottis is wider than the subglottis/cricoid ring [4]. This variation based on dynamic changes is apparent through review of literature where studies have differed on which site in the airway is considered the narrowest point. In non-dynamic evaluations such as cadaver studies and computed tomography (CT) scans, the subglottis is the narrowest point [4,6–8]. In studies utilizing techniques that allow for dynamic changes that account for variations during respiration, such as magnetic resonance imaging (MRI) and video-bronchoscope imaging, the vocal cords are recorded as the most narrow point [3,4,9]. Meanwhile, the subglottic region is the narrowest

* Corresponding author. 150 Academy St, Newark, DE, 19716, USA
E-mail address: cfromen@udel.edu (C.A. Fromen).

<https://doi.org/10.1016/j.combiomed.2022.106058>

Received 9 June 2022; Received in revised form 3 August 2022; Accepted 27 August 2022

Available online 5 September 2022

0010-4825/© 2022 Elsevier Ltd. All rights reserved.

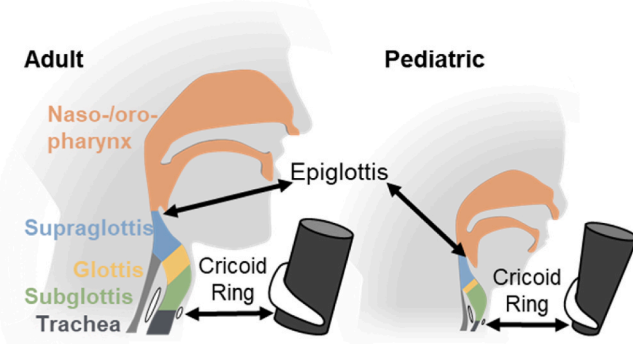


Fig. 1. Anatomical overview diagram of the adult and pediatric airways. Depicted regions of interest include the naso-oro-pharynx (orange), supraglottis (blue), glottis (yellow), subglottis (green), and trachea (grey), as well as notable variations of anatomical features, the epiglottis and cricoid ring shape.

“functionally” based on intubation *in vivo*, as the passing tube dilates the mobile vocal cords but cannot dilate the fixed cricoid ring [8]. With growth of the child, the cricoid ring expands and becomes cylindrical, meaning that when the vocal cords dilate (abduct), the vocal cords remain the narrowest point [4].

Given the notable changes occurring in upper airway structure, it is highly likely that these structural changes provide significant impact to local and downstream airflows. For example, the narrowing of the glottis relative to the cricoid ring area as well as the funnel shape or cylindrical shape of the cricoid ring area are expected to influence the flow pattern downstream of the glottis where narrowing airways focus the flow to form a high-speed jet, called the glottal jet [5,10]. Turbulence, recirculation regions, and fluidic phenomena such as the glottal jet are expected to be different between adults and pediatric patients owing to differences in geometry [10]. However, the extent of those differences and the transition of metrics from “pediatric”-like values to “adult”-like values during development are not well quantified. Investigation of pediatric airways in general remains challenged by the availability of anatomically accurate CT-based models, with many aerosol studies focusing on idealized models or representative models of a single age group [11–15]. Studies on infants ages 0–3 have investigated the role of developmental changes within the nasal passages and lower airway geometry on deposition following nose breathing, as well as inter-patient variability of lower lungs or upper airway airflow within 5-year-olds [12,16–18]. However, thorough evaluation of how the known changes within the upper airway influence local and downstream aerosol deposition has yet to be performed [2,14]. As a 6-year-old is more likely to be undergoing upper airway development than their younger counterparts, it is expected that inter-patient anatomical variability would play a significant role in the efficacy of current aerosol therapeutics and treatment paradigms. For example, a subject with a more “adult”-like pediatric upper airway may be suited for an inhaler and spacer, which can require high peak inspiratory flow rates and deliver larger particles, while a subject with a more “pediatric”-like upper airway may benefit more from a nebulizer, which typically has lower flow rate requirements, delivers smaller aerosols, and have been shown to be more efficacious in pediatric subjects [19–21]. Such studies would inform pharmaceutical design and guide prescriptions of current aerosol therapeutics and devices.

This work provides details of aerosol deposition in the upper airways of two healthy 6-year-old pediatric subjects, *i.e.*, one male and one female, using computational fluid-particle dynamics (CFPD) simulations. The purpose of this work is to evaluate aerosol deposition in airways reconstructed from subject CT scans in a previously understudied age group, 6-year-olds, and evaluate the role of varied anatomic developmental differences on local and downstream aerosol deposition. In addition to the two 6-year-old subjects, an open access idealized

pediatric upper airway model provided by the Respiratory Drug Delivery (RDD) society, which was based on previously developed idealized models, was utilized as a comparison [22–24]. Anatomical geometries and fluid-dynamic features were quantified to assess the developmental state of each subject. Particle deposition was correlated to relevant parameters, including particle diameter, flow rate, anatomical features, and the impaction parameter. The relationship between quantified developmental states and the impact on particle deposition trends as a function of the above parameters was addressed and utilized to better understand the relationship between anatomical development and aerosol deposition. Finally, a clinically applicable example was demonstrated using a model polydisperse particle size distribution mimicking a pharmaceutical aerosol based on the Advair® Diskus® to inform predictions of patient efficacy disparities. With this limited but representative patient-derived dataset, we aim to provide insight into pediatric development while building a platform for future work of upper airway deposition on understudied pediatric age groups.

2. Methods

2.1. IRB approval and ethical considerations

A dataset of healthy pediatric patient CT scans was originally obtained through a prior study exempt from consent under Internal Review Board (IRB) approval and used retrospectively in this work. Subjects were exempt from consent under Category 4 of secondary studies on deidentified data. Access to these CT records was obtained through approval through the University of Delaware and Nemours Children’s Hospital - Delaware IRB Review. No new data or information were collected from the human pediatric subjects involved in this work. Subject CT scans have been deidentified such that the information known to the primary researchers are the CT scan data, patient age, and patient sex. Subjects have been assigned an identification number for internal reference.

2.2. CT reconstruction and mesh generation

The entire workflow is visually depicted in Supplemental Fig. S1. Two CT scans of 6-year-old subjects, one male and one female, were converted to 3D renderings using Materialise Mimics (Materialise, Leuven, Belgium), which is a common practice in respiratory upper airway modeling [25]. An idealized model was rendered based on a model provided by the Respiratory Drug Delivery (RDD) society and inverted such that the airways, as opposed to the airway walls, were utilized. This model, from Wachtel et al. [26], is an open access model inspired by the Alberta Idealized Throat (AIT) for pediatric subjects. The comparison of this model to the AIT pediatric model is described in more detail in Supplemental Methods, Supplemental Fig. S2, and Supplemental Table S1. No smoothing was performed on the CT scans. While it is known that jagged topology of CT scan derived models lack wall-layer local fluid flow accuracy as *in vivo* structures are much smoother and more similar to an idealized model, it is also known that CT derived models benefit from accuracy in anatomical structures and intersubject variability [27]. To avoid outlet flow anomalies, the trachea of all three models was extended in SolidWorks (SolidWorks Corp., Waltham, MA) by converting the outlet to a sketch and extruding the sketch by a distance of 10x the hydraulic diameter of the trachea. Renderings were exported from SolidWorks as STL files and converted to STEP files in Autodesk Netfabb (Autodesk Inc., San Rafael, CA). These renderings were meshed using Ansys Fluent Meshing (Ansys, Inc., Canonsburg, PA, USA). Each rendering was meshed to varying degrees of elements by tuning the element size and utilizing adaptive meshing. Thus, for each rendering, five meshes were created ranging from <100 k elements to >500 k elements at a minimum, specific values for mesh sizes in the legend of Supplemental Fig. S3. Fluent CFPD experiments were performed on each mesh at 15 Lpm with 1 μ m particles. Cross sections were

taken along an axis, and the axis was selected by quantifying the projection of the model in each axis. Cross sections were taken at the point related to anatomical features at 1) the model inlet, 2) the naso-oropharynx-supraglottis interface, 3) the supraglottis-glottis interface, 4) the point in the glottis with the smallest diameter (i.e., Distance = 0 mm), 5) the glottis-subglottis interface, 6) the subglottis-trachea interface, and 7) the model outlet. A line across the midpoint of each cross section was created. The velocity magnitude along the line was reported. This process was repeated for each of the five meshes, and the resultant velocity magnitude graphs were overlaid, as can be seen in [Supplemental Fig. S3](#). It was determined that the minimal variability in velocity profile with increasing element count suggested that the models were mesh independent. Additionally, though no prism layers were employed, the y -plus values for the models were such that 98% of values were less than 10 and 38% of values were less than 1.

2.3. Anatomical analysis

CT scans of the two subjects were reviewed by a radiologist and otolaryngologist to confirm the models were representative of healthy subjects. The otolaryngologist further delineated key anatomical features of interest from the CT scans, including the naso-oropharynx (orange), supraglottis (blue), glottis (yellow), subglottis (green), and trachea (grey). These CT annotations were then translated to the models and their respective centerlines. To accomplish this, the model was resliced in the CT-scan axis (the z -axis) at intervals equivalent to the CT scan intervals, and the features of interest were identified. These features were given relative coordinates to the model midpoint, and the z -axis relative coordinates were correlated to that of the centerline coordinates in the z -axis. However, the region denoted as the subglottis by the otolaryngologist was extended when correlating to the centerline coordinates to account for the continued decreasing diameter of the model that suggested the continuation of the subglottis (see Supplemental Methods and [Supplemental Fig. S4](#) for more information). Thus, the CT scan z -axis was translated to the centerline z -axis to allow for anatomical regions of interest to be identified during analysis involving the centerline. Additionally, a similar analysis was performed on the idealized model using the anatomical description by Golshahi *et al.* [22]. The model diameter at these anatomical features was analyzed such that the glottis narrowest point (red dashed line and distance through model of 0, as can be seen in [Fig. 2](#)) was compared to the cricoid ring area (white dashed line) to determine the relative narrowest feature between the two. Additionally, the change in model diameter was used to determine if the subglottis and cricoid ring areas were funnel-shaped or cylindrical. A decrease in model diameter near the cricoid ring suggested a funnel-shape while a constant diameter suggested a cylindrical shape. Finally, the angle of the epiglottis (black dashed line) relative to the trachea was measured to evaluate if it was more acute ($<30^\circ$) or more obtuse ($>35^\circ$) for the expected range of 20 – 45° . This angle was measured by setting an average plane through the trachea, setting the midplane of the epiglottis, and measuring the angle between the two planes at the center of the model (see [Supplemental Fig. S5 A-C](#)).

2.4. Anatomical developmental characterization

The assessment of “pediatric”-like and “adult”-like anatomical characteristics consisted of three criteria: the narrowing of the glottis and cricoid ring area, the funnel or cylindrical shape of the cricoid ring area, and the angle of the epiglottis. The narrowest point for an adult subject was considered to be the glottis, but the narrowest point for the pediatric subjects was considered the subglottis or cricoid ring area. The subglottis and cricoid ring areas were considered funnel-shaped for pediatric subjects and cylindrical for adults [28]. Finally, the angle of the epiglottis was considered to be more acute when the larynx sits lower in the neck in adult subjects and more obtuse when the larynx sits

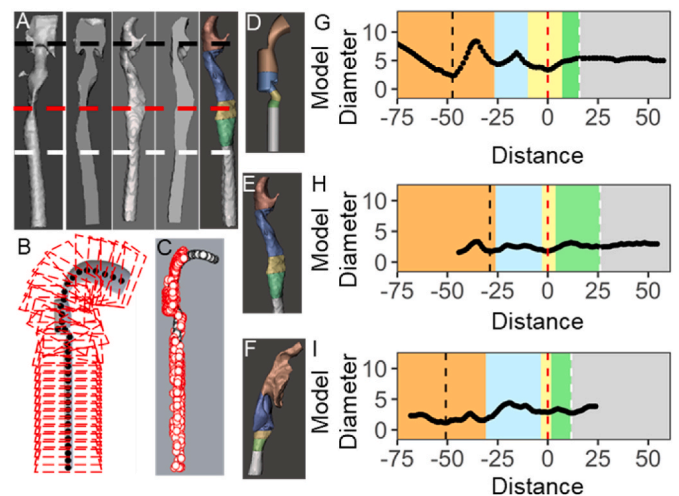


Fig. 2. (A) From left to right, the front view, front cross section, side view, side cross section, and the corresponding anatomical features colorized for Subject A with dashed lines representing the epiglottis (black), glottis (red), and cricoid ring area (white). (B) A centerline schematic for the idealized model represented as black dots with planes shown as red dashed squares and (C) the actual centerline shown in black dots with deposition data shown in red for CFPD at 120 Lpm and $10\ \mu\text{m}$. (D–F) The 3D models and (G–I) the corresponding graphs highlighting the naso-oropharynx (orange), supraglottis (blue), glottis (yellow), subglottis (green), and trachea (grey) for all three models: the idealized model (D, G), CT based model Subject A (E, H), and CT based Subject B (F, I). Graphically displayed is the distance through the model along the centerline versus the model diameter with the color-coordinated highlighting of anatomical features as stated above and dashed lines indicating the epiglottis (black), glottis narrowest point (red) and cricoid ring area (white).

higher and more anterior in pediatric subjects [28]. These anatomical variations influence the epiglottis angle such that an angle of 20° was considered average for an adult while an angle of 45° was considered average for a pediatric subject [4,29]. Our assessment determined if the measurements were more acute (“adult”-like) or obtuse (“pediatric”-like). The anatomical feature characterization is summarized in [Table 1](#).

2.5. Centerline generation

Lung model centerlines were determined via an in-house modification of the open-source program PyRaabe (v0.1.0) [30,31]. By default, PyRaabe takes an STL file as input and returns the model’s centerlines, average dimensions, and connectivity. It is based on the Vascular Modeling Toolkit (VMTK, [vmtk.org](#)), which derives the centerlines from the Voronoi diagram of the model using an algorithm that is stable in the presence of surface variations. The program was modified to additionally return the coordinates and maximum inscribed sphere radius of each point from the computed centerlines. This information was used to determine the normalized position of the regions of interest within each airway and quantify local variations in airway diameter. The distance between two points was used to calculate the length of the centerline in units of mm. Furthermore, these modifications permit the use of a

Table 1
Comparison of “pediatric”-like and “adult”-like features of the three 3D models.

Feature	Pediatric	Adult	Idealized	Subject A	Subject B
Narrowing	Narrowest at Cricoid Ring	Narrowest at Glottis	Adult	Adult	Pediatric
Cricoid Ring Shape	Funnel Shape	Cylinder Shape	Adult	Pediatric	Pediatric
Angle of Epiglottis	45°	20°	30°	45°	35°

graphical user interface to access the primary functionality of PyRaabe and the extended features described here. The source code used for the in-house modifications is available at <https://github.com/fromenlab/pyraabe-fromen>. It is important to note that the resultant distance measurement is not equivalent to the distance in any axial measurements, nor is it equivalent to the CT slicing distance, but it is instead a distinct method of quantifying a path through an airway.

2.6. CFPD governing equations

Ansys Fluent 2021 R1 (Ansys, Inc., Canonsburg, PA, USA) was utilized for the CFPD simulations. The Euler-Lagrange method enhanced with in-house C programs was employed to simulate airflow, particle transport, and particle deposition in all three airway models generated [32]. The transition shear stress transport (SST) model was employed to resolve the transitional airflow regimes between laminar and turbulence. The airflow field was assumed to be unsteady and driven by pressure differences and was additionally assumed to be incompressible. Gravity was defined by generating an averaged vector based on the model wall, taking the negative of the average vector, and multiplying by the scalar value for the gravitational constant 9.81 m/s^2 . By doing this, gravity was applied as a vector in a direction opposite to the overall model. Thus, regardless of the orientation of the model, gravity was opposite of the normal projection of the model or mimicking an upright sitting position [33]. The conservation laws of mass and momentum, applicable for both laminar and turbulent flows [34], can be written in tensor forms as follows:

$$\frac{\partial u_i}{\partial x_i} = 0 \quad (1)$$

$$\frac{\partial u_i}{\partial t} + u_j \frac{\partial u_i}{\partial x_j} = -\frac{1}{\rho} \frac{\partial p}{\partial x_i} + \frac{1}{\rho} \frac{\partial \tau_{ij}}{\partial x_j} + g_i \quad (2)$$

where u_i represents the fluid velocity, p is the pressure, g_i is gravity as described above, and viscous stress tensor τ_{ij} in Equation (2) is given by:

$$\tau_{ij} = \mu \left[\left(\frac{\partial u_i}{\partial x_j} + \frac{\partial u_j}{\partial x_i} \right) - \frac{2}{3} \delta_{ij} \frac{\partial u_k}{\partial x_k} \right] \quad (3)$$

Particles were assumed to be spheres with a high particle-to-air density ratio and negligible thermophoretic forces; this reduced the particle trajectory equation to the following:

$$\frac{d}{dt} (m_p u_i^p) = F_i^D + F_i^L + F_i^{BM} + F_i^G \quad (4)$$

where u_i^p is the particle velocity, m_p is the particle mass, F_i^D is the drag force, F_i^L is the Saffman lift force, F_i^{BM} is the Brownian motion-induced force, and F_i^G is the force of gravity. In-house user-defined functions (UDFs) were utilized to define the Brownian motion-induced force as implemented by Feng et al. [32]. Additional details on these CFPD models and equations, including the effects of turbulence on particle trajectory, can be found in Chen et al. and related works [34–37].

2.7. CFPD assumptions and parameters

Particles were released from the inlet via file injection, allowing for the definition of the velocity direction and magnitude, the particle diameter, and the separation of particles into three files for triplicate analysis. To accomplish this, particles were first released and immediately captured by setting the inlet as a capture zone. Then the data of the captured particles were exported, manipulated, and divided into three sets of files per model. Particle release velocity was assumed to be equivalent to the theoretical average velocity of the airflow and uniform across the inlet. Particle diameter d_p was varied from 100 nm to 10 μm , and the particle density ρ_p was consistently 1000 kg/m^3 . The model exhalation flow rate Q_{in} was varied from 10 to 120 Lpm by calculating

the outlet area of each model and dividing to determine the velocity. The boundary conditions used can be summarized as follows:

1. Outlet velocities were calculated based on each model trachea cross-sectional area and the flow rate.
2. Inlet pressure at the naso-oropharynx was assumed to be open to the atmosphere and set to 0 gauge PSI.
3. Particles were released at the inlet with defined position, velocity, and diameter and were dilute (1E-19 kg/m^3).
4. Particle-wall interaction boundary condition was assumed to be a “100% trapped wall,” meaning the airway will capture particles at initial contact.

The particle velocity, diameter, and physical characteristics, as well as the fluid assumptions of flow rates, inlet and outlet pressure and velocity boundary conditions, and the trapped wall particle-wall interaction condition were assumed based on previous research [32,34,38]; however, the range of flow rates and the triplicate file injection method for particle tracking was adapted from previous research to allow for the unique analysis in this work. Particle deposition results were reported as the exported coordinate positions of deposition for further analysis. Additionally, turbulence intensity, Reynolds number, and the axial and tangential velocities were reported along the z-axis. Measurements of turbulence intensity, Reynolds Number, and the axial and tangential velocities were taken at the glottis by creating a cross section at the z-axis coordinate, which corresponded to the narrowest point in the glottis. Finally, the glottal jet length was measured by the difference in z-coordinate between the top and bottom of the glottal jet as defined by the velocity at half of the maximum velocity of the glottal jet at either end and confirmed visually. The glottal jet length was reported as normalized to the average trachea for comparisons between models.

2.8. Fluid-dynamic developmental characterization

The assessment of “adult”-like or “pediatric”-like fluid-dynamic characteristics consisted of three criteria: The peak intensity of turbulence, the length of the glottal jet, and the peak intensity of the turbulent Reynolds number. The intensity of turbulence was qualitatively assessed as being high or low by quantifying the peak turbulence intensity through the model. The turbulence intensity is defined by Ansys Fluent as a relationship between the square root of the turbulent kinetic energy divided by a reference velocity; this metric was selected to assess turbulence because it is dimensionless and includes reference velocity, allowing for unbiased comparisons between models. A high turbulence intensity was expected of a pediatric patient [10,12]. Reynolds numbers that were in a range below 1250 suggest a low turbulence model and were considered “low” and “adult”-like while anything above that range would be considered “high” and “pediatric”-like [10]. The glottal jet length was measured by finding velocities averages equivalent to half of the maximum velocity in a glottal jet cross section [5]. This length was compared to the trachea diameter and reported as the ratio of the glottal jet length to the trachea diameter for each model. This ratio is expected to be high for adults as adults are expected to have a long glottal jet. A glottal jet ratio above 5 was considered “high” or “adult”-like and below 5 was considered “low” or “pediatric”-like [5,12]. Finally, the turbulence intensity was evaluated as the peaks in turbulence intensity and expected to have peaks at values of 2 or below for “adult” throats, which are considered here to be “low” values, and anything above 2 was considered “high” or “pediatric”-like [5,12].

2.9. Particle deposition analysis

Particle deposition data exported as coordinates of deposition were compiled in Microsoft Excel (Microsoft Corporation, Redmond, WA) spreadsheets which were read and analyzed using Matlab (MathWorks, Natick, Massachusetts). The points of the centerline of the model were

used to create vectors, which were then employed to create planes using a point and vector definition of a plane, effectively slicing the model as a function of distance along the centerline. For example, point *A* and point *B* were used to create a vector defined by $\nu = B - A$. The definition of the plane *P* based on the vector ν and point *B* followed the point-normal equation $0 = \nu \cdot (P - B)$. Thus, a plane normal to the vector between two points of the centerline and located tangent to the second point was created. All particles with deposition coordinates greater than the plane were counted and removed. Upon creating the next plane and counting particles, only particles greater than the next plane were counted, and there was no overlap in counted particles between planes due to removing particles that were successfully counted. There were approximately 100 planes per model with the distance between planes ranged from 0.8 to 1.5 mm and variation within the model was within 0.5 mm throughout the centerline. Exact plane spacings are reported in [Supplemental Table S2](#). The particles counted were normalized to the particles which entered the model and were subsequently averaged for the three particle injections, resulting in the Average Deposition Fraction (Av. Deposition Fraction). This was frequently utilized to compare parameter variations within an individual model; however, compared to between models, the surface area available for deposition was taken into consideration. Deposition results were reported by first taking the particle counts in each anatomical region and calculating the average deposition fraction for each region (as opposed to counts between each plane) and then scaling by a factor of $(1 - A_s / A_t)$ where A_s is the surface area of the region and A_t is the total surface area of the model, effectively normalizing to the inverse of the surface area. The result is a metric that reflects the average deposition fraction but accounts for larger surface areas having more potential sites for particle deposition, as well as scaling between model area totals to allow for the comparison between models.

2.10. Pharmaceutical approximation

For a clinically relevant pharmaceutical model, particle diameters were adjusted to match the distribution of the Advair® Diskus® immediately upon release from the Diskus apparatus such that no airway replica or induction port would skew the particle size distribution due to deposition. The distribution, reported by Ali et al., was translated to the particle counts for each model, such that the resulting model distribution matched the reported distribution (see [Supplemental Table S3](#)) [39–41]. The particle size distribution is thus a reflection of the distribution reported for the Advair® Diskus® and translated to a dilute phase, which is a simplistic approximation of a pharmaceutical particle distribution but lacks representation of drug composition and inhaler apparatus. Additionally, the particle velocities and CFPD model velocities were adjusted to reflect a flow rate of 81 Lpm, which is the flow rate reportedly required to actuate the Advair® Diskus® [20,42,43]. Results were reported as deposition coordinates and analyzed to reflect known literature values including the Upper Throat Region (UTR) deposition, Total Lung Dose (TLD) escaped at the outlet, and the Delivered Dose (DD) which is the total between the UTR and TLD (i.e., all particles that enter the model and do not escape via the inlet) [20,42–44]. Additionally, the size distribution of particles at the outlet was quantified as the mass median aerodynamic diameter (MMAD) and compared against literature values [20,42–44]. While this model is a simplistic representation of an inhalable pharmaceutical, it provides fundamental knowledge of realistic particle distribution behavior as well as a framework for future studies intended to inform therapeutic design.

2.11. Model validation

The idealized model *in silico* data were compared to *in vitro* data from Golshahi et al. [22], and thus the range of flow rates used in that work were included in this work; namely a range of 30 Lpm to 120 Lpm [22]. For pediatric subjects, peak inhalation flow rates can reach into the

hundreds and it is expected that a pediatric patient who is prescribed the Advair® Diskus® is capable of actuating the inhaler at the minimum flow rate required, 81 Lpm; thus, flow rates of 90 and 120 Lpm are representative of values expected under forced breathing conditions [43, 45]. Flow rates during tidal breathing for a pediatric subject are typically much below this range at 10–15 Lpm [15,46]. Thus, the range used in this paper included low tidal breathing flow rates (10 and 15 Lpm) and high forced breathing flow rates (90 and 120 Lpm), as well as values in between that are typically evaluated for adult subjects and are common for aerosol studies (30 and 60 Lpm) [47,48]. To accurately evaluate the range of possible flow rates for a pediatric subject, we have included flow rates from 10 to 120 Lpm. Particle sizes were selected such that a range of $d_p^2 Q$ comparisons could be made and indicated that the fraction of deposition was comparable between the *in silico* and *in vitro* data; suggesting that this model is accurate and applicable (see [Supplemental Fig. S2](#)). Model comparison of *in silico* and *in vitro* data was performed for the idealized model [22] and the CFPD model employed in this study has been well validated on the predictability of (1) laminar-to-turbulence transitional pulmonary airflow field (for Transition SST Model) [32], and inhaled particle deposition (Euler-Lagrange model) [49].

2.12. Statistical methods

Particle deposition coordinates were exported from Fluent and analyzed along the centerline as described in “Centerline Generation” above. The number of particles depositing was divided by the total number of particles which entered the model, resulting in the reported metric being a normalized value referred to as the average deposition fraction. The combined total number of particles depositing on the model divided by the total that entered the model was reported as the Upper Throat Region deposition (UTR). Both the average deposition fraction and UTR data were not normal distributions and the factors influencing these metrics which were desired to statistically analyze included flow rate, particle diameter, model, and anatomy region; however, there is not a non-parametric test capable of such multivariate analysis and it is thus recommended to include combinations of one-way nonparametric tests along with multivariate parametric tests to determine which factors are significant. To this end, four tests were used: 1) a series of Kruskal-Wallis nonparametric one-way ANOVA tests, 2) a robust parametric ANOVA, 3) a Tukey’s Honest Significant Difference (Tukey’s HSD) post-hoc adjusted parametric ANOVA, and 4) a multivariate estimated marginal means regression analysis. Resulting p-values from the Tukey’s HSD adjusted ANOVA to compare the influence of diameter and flow rate on UTR are reported in [Supplemental Fig. S6](#). Statistical parameters including p-values and F-values for the Kruskal-Wallis ANOVAs and robust two-way ANOVAs comparing the influence of diameter and flow rate on UTR are reported in [Supplemental Table S4A](#). Regression results are utilized to visualize results of the KW, robust, and Tukey’s HSD adjusted ANOVAs and can be seen in [Fig. 8](#). Additional tests performed to compare the influence of anatomical region on deposition and to compare the influence of $d_p^2 Q$ and model utilized on average deposition fraction are reported in [Supplemental Tables S4B and S4C](#), respectively. Additionally, Student T-tests were used when comparing the pharmaceutical model results and are reported in [Supplemental Table S4D](#). All statistical tests are reported in corresponding figure captions and performed as indicated throughout the text. All p-values calculated less than 0.00001 are reported as $p < 0.00001$.

3. Results

Centerline quantification of the reconstructed and annotated models allowed for model diameter measurements to be graphed against the distance along the centerline ([Fig. 2](#)). The naso-oropharynx (orange), supraglottis (blue), glottis (yellow), subglottis (green), and trachea (grey) were identified by anatomical annotations and correlated to the

centerlines; anatomical sections are color coordinated between the model sections (Fig. 2D, E, and F) and depicted graphically (Fig. 2G, H, and I). The narrowest point within the glottis was chosen as a common reference to account for different airway volumes between models and is indicated both by a dashed red line and by distance through the model of 0 (see Fig. 2). The model diameter at this point was compared to the cricoid ring area, indicated by a dashed white line.

Based on the anatomical measurements, we assessed the “pediatric”-like and “adult”-like features of the model following three criteria: the narrowing of the glottis and cricoid ring area, the funnel or cylindrical shape of the cricoid ring area, and the angle of the epiglottis (Table 1). For the idealized model, the glottis has a smaller model diameter than the cricoid ring area, suggesting that this is the relatively narrowest location. This is also true of model Subject A; however, model Subject B displayed the opposite trend. In model Subject B, the model diameter is smaller in the cricoid ring area than the glottis area, suggesting that the relative narrowest location in this model is the cricoid ring area. Additionally, the model diameter gradually decreases between the subglottis and the cricoid ring area for both models Subject A and Subject B. This gradually decreasing diameter suggest that the cricoid ring area is funnel-shaped for both models. The idealized model does not display this trend but instead has a constant model diameter in the cricoid ring area, suggesting that this feature is cylindrically shaped. The angle of the epiglottis is the last measurement of the anatomical features (see Supplemental Fig. S5 A-C for method). An angle of 20° is considered average for an adult while an angle of 45° is considered average for a pediatric subject [4,29]; here, we find that model Subject A has an epiglottis angle of 45° and is a “pediatric”-like feature, however models Subject B and the idealized model fall between the range specified. The idealized model has an angle of 30° , which is closer to “adult”-like than to “pediatric”-like. Model Subject B has an angle of 35° , which is closer to “pediatric”-like than “adult”-like. However, it is known that the epiglottis varies significantly from subject to subject and is difficult to characterize developmentally. The above metrics described as the relationship between the narrowest points in the glottis and cricoid ring, the shape of the cricoid ring area, and the epiglottis angle are all summarized in Table 1 to visualize the “adult”-like and “pediatric”-like features of each model. It is important to note that these two geometries displayed physical features that fall within characteristic features of healthy 6-year-old pediatric patients [8,9]; thus, we believe that these two representative geometries are not extreme outliers of this population.

Based on literature data comparing pediatric to adult upper airways

in CFPD, it would be expected that the pediatric airways would have more turbulence, more recirculation flow, and higher Reynolds number in comparison to the adult airways at the same inhalation flow rate [2,5,10,50]. Models were compared at a physiologically relevant flow rate of 15 Lpm, representative of tidal breathing, and these relevant fluid-dynamic metrics were assessed. Here, turbulence was measured as turbulence intensity along the z-axis as reported from Ansys Fluent. From Fig. 3 it is evident that the peak turbulence intensity is higher in model Subject B than Subject A and the idealized model. Recirculations were measured as a ratio between the axial and tangential velocity, which were also apparent greater for Subject B than Subject A and the idealized model. The axial flow relative to the tangential flow provides a metric to assess how much the fluid is flowing against the bulk fluid flow pattern. Recirculations inherently require flow perpendicular to the flow pattern and while this does occur in non-recirculatory flow also, the increase in opposing flow relative to tangential flow provides a critical metric to assess how significant this phenomenon is relative to bulk flow motion [5,10]. A significant peak in axial velocity relative to tangential velocity indicates a recirculation region. This can be visualized in Fig. 4, where the tangential velocity is shown as contours and the axial velocity is shown as arrow velocity vectors. There is visually more axial flow in Subject B cross sections compared to those of Subject A and the idealized model. While there are some visually apparent axial and tangential flows in Subject A, the overall trend is much more similar to the idealized model than it is to Subject B; there are minor fluctuations across the surface in tangential flows and nearly negligible axial flows. This is reflected graphically as well in Fig. 3, where the peak in the ratio of axial velocity to tangential velocity is most significant in the supraglottis of Subject B. Additionally, the Reynolds number is less variable between models but is greatest in model Subject B, as assessed at a normal tidal breathing flow rate of 15 Lpm. An increase in Reynolds number is expected for pediatric subjects compared to adults, as a higher velocity is required to maintain the same tidal breathing flow rate with a geometrically smaller airway. Measurements of the resultant glottal jet further confirmed deviations between the three models. The length of the glottal jet was measured by quantifying two points along the x-axis above and below the glottal jet, where the velocities surrounding the glottis were half of the maximum velocity through it based on a total inlet flow rate of 15 Lpm for normal tidal breathing. The visualization of this measurement, can be seen in Supplemental Fig. S5 D-F, along with the corresponding pressure gradient in Supplemental Fig. S5 J-L. This length was then compared to the trachea diameter of the model and the reported value is the ratio of the glottal jet length to the trachea

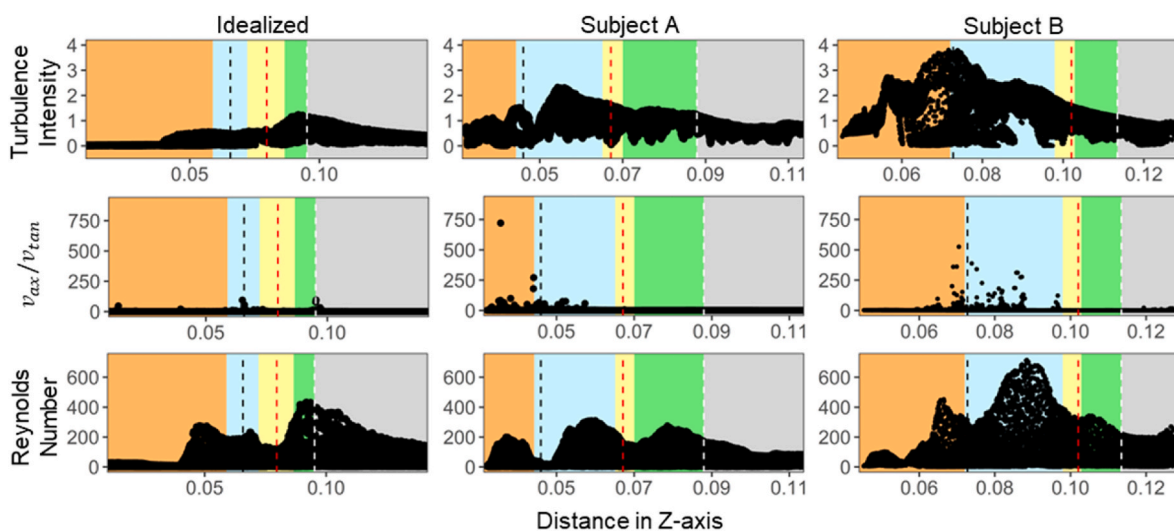


Fig. 3. The turbulence intensity (top row), axial velocity to tangential velocity ratio (middle row) and the Reynolds Number (bottom row) for the idealized model (left), Subject A (middle) and Subject B (right). Results for a flow rate of 15 Lpm.

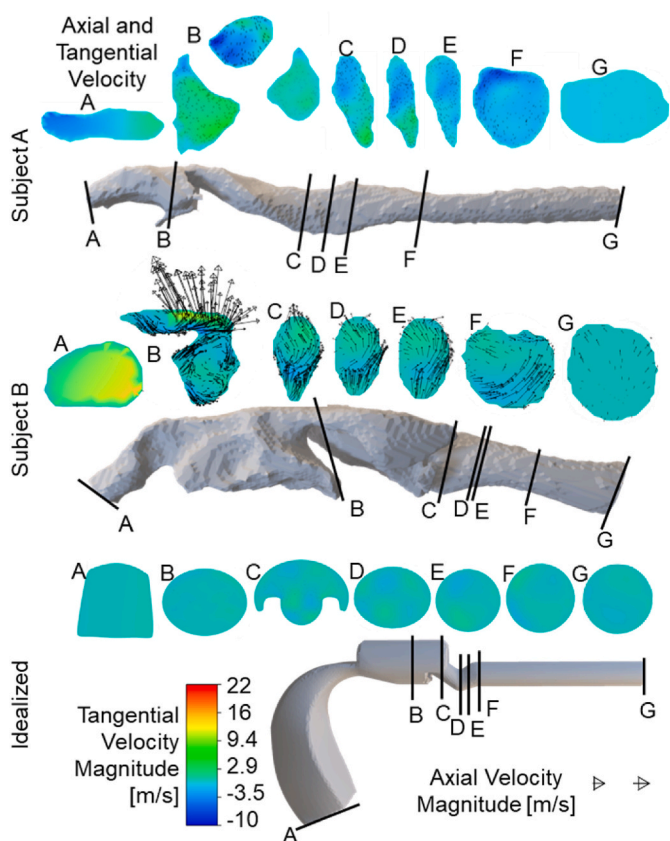


Fig. 4. Axial and tangential velocities visualized at cross sections along the airways at regions of interest: A) the model inlet, B) the naso-oropharynx-supraglottis interface, C) the supraglottis-glottis interface, D) the point in the glottis with the smallest diameter (i.e., Distance = 0 mm), E) the glottis-subglottis interface, F) the subglottis-trachea interface, and G) the model outlet. Tangential velocities are represented by contours, while axial velocities are represented by arrow velocity vectors, both of which are plotted in the same fixed range across all three models. These were shown for Subject A (top), Subject B (middle), and the idealized model (bottom). Results for a flow rate of 15 Lpm. Additionally, pressure gradient visualization is provided in Supplemental Fig. S5.

diameter (see Supplemental Table S5). The length of the glottal jet is expected to be smaller in pediatric subjects compared to adult subjects; a ratio greater than 5 was considered more “adult”-like and less than 5 was considered more “pediatric”-like. Subject A and the idealized model exhibited longer glottal jets, while Subject B had the smallest glottal jet assessed at a flow rate of 15 Lpm, representative of normal tidal breathing. A summary of these findings is presented in Table 2. Thus, in all aspects of fluid dynamics, model Subject B is qualitatively exhibiting more “pediatric”-like tendencies than the idealized model or Subject A, which both behaved more similarly.

Table 2

The fluid dynamic metrics of interest (turbulence intensity in the glottis, normalized glottal jet length, and the Reynolds number) expectations for a pediatric and adult subject, as well as the resulting measurements for the three models (idealized model, Subject A, and Subject B) indicating if the result was a “pediatric”-like or “adult”-like feature.

Feature	Pediatric	Adult	Idealized	Subject A	Subject B
Turbulent Intensity in Glottis	High	Low	Low	Low	High
Normalized Glottal Jet Length	Low	High	High	High	Low
Reynolds Number	High	Low	Low	Low	Low

Particles entered the model at the inlet in a dilute phase, particle diameter (d_p) and velocity were varied between experiments, and the resulting trends in deposition were analyzed for differences in total and spatial deposition. Particle diameters were adjusted to be 100 nm, 500 nm, 1 μ m, 3 μ m, 5 μ m, and 10 μ m, spanning a range of relevant inhalable sizes, and the inlet velocities were also varied to study a flow rate range of 10 Lpm, 15 Lpm, 30 Lpm, 60 Lpm, 90 Lpm, and 120 Lpm. Total deposition in the model (in the upper throat region – UTR) ranged from 0% to 100% average deposition fraction across the range of d_p and flow rate studied, as shown for each model in Fig. 5. Representative naso-oropharynx deposition on the models is visualized in Supplemental Fig. S5 G-I for a flow rate of 15 Lpm and a particle diameter of 1 μ m. At a high level, increasing UTR deposition was observed for both increasing d_p and flow rate, in line with expectations based on literature [22,47]. Across the three models, UTR deposition appeared similar between Subject A and the idealized model, while noticeable variations appeared for Subject B. A Kruskal-Wallis one-way ANOVA corroborates that model ($p = 0.019$) is in fact a significant variable, pointing to the importance of considering individual geometries in predicting UTR deposition. A regression analysis across all three models predicting UTR deposition as a function of d_p and flow rate is visualized in the far right plot of Fig. 5, highlighting the general UTR deposition dependency on increasing d_p and flow rate.

In line with the UTR results, the resulting regional analysis showed increasing deposition as d_p increased in all models (see deposition along the centerline of varied d_p in Fig. 6). While increasing d_p increased deposition overall, there was a statistically significant difference in particle deposition patterns between d_p of 1 μ m and 3 μ m, such that the larger d_p had significantly more deposition in the UTR than the smaller d_p . A Kruskal-Wallis one-way ANOVA indicated that the d_p was a significant factor ($p < 0.00001$) in variations in UTR. Two robust two-way ANOVAs comparing flow rate and diameter ($p < 0.00001$) and comparing model and diameter ($p < 0.00001$) to UTR both indicated that d_p was a significant factor, even when accounting for interactions with other parameters. A Tukey’s HSD post-hoc adjusted multivariate ANOVA between flow rate, d_p , and model to UTR are reported in Supplemental Fig. S6 and indicate that there is significant difference in UTR between particles that are 1 μ m and 3 μ m. The increase between these two d_p can be seen in Fig. 6 at a flow rate of 30 Lpm, a flow rate slightly above tidal breathing for an average 6-year-old [15,46], where increased deposition was observed in all models predominantly above the glottis. This significant variation in UTR as a function of d_p between the 1 μ m and 3 μ m also emerged in the overall multivariate regression in Fig. 5 (right).

Similarly, the resulting regional analysis as a function of flow rate showed similar deposition trends to the overall UTR data (see deposition along the centerline of varied flow rates in Fig. 7). The shown flow rates of 15 Lpm and 90 Lpm in Fig. 7 represent normal tidal breathing and forced breathing for a pediatric subject, respectively [15,45,46]. While total UTR deposition slightly increases with increasing flow rate, the relationship between flow rate and UTR deposition is less significant than other parameters. A series of Kruskal-Wallis one-way ANOVAs indicate that flow rate is not significant ($p = 0.112$) across all models, while d_p ($p = 1.948e-13$) and model ($p = 0.019$) are significant. Two robust two-way ANOVAs indicate both d_p ($p < 0.00001$) and flow rate ($p = 0.00002$) are significant, but importantly the higher F-value of d_p ($F = 49.58$) compared to flow rate ($F = 7.23$) confirms that d_p is the more significant parameter. The Tukey’s HSD post-hoc ANOVA analysis reported in Supplemental Fig. S6 indicates that there are very few instances where flow rate variations have significant influence on UTR deposition. Finally, in the regression analysis visualized in Fig. 5 consistently demonstrates low slopes for UTR as a function of flow rates for the six d_p analyzed, especially in the idealized model and Subject A models. In contrast, the position of these six regression lines increases as the represented d_p increases, supporting that flow rate is not a significant factor compared to d_p . Additionally, UTR as a function of d_p shows

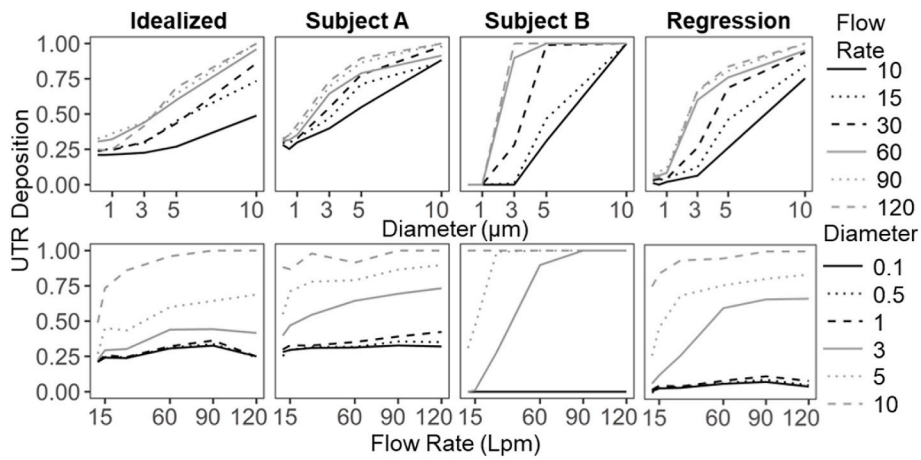


Fig. 5. The model UTR deposition for the idealized model, Subject A, and Subject B and the predicted UTR deposition based on a multivariate regression analysis as a function of diameter (top row) plotted for each flow rate, as well as a function of flow rate (bottom row) plotted for each particle diameter.

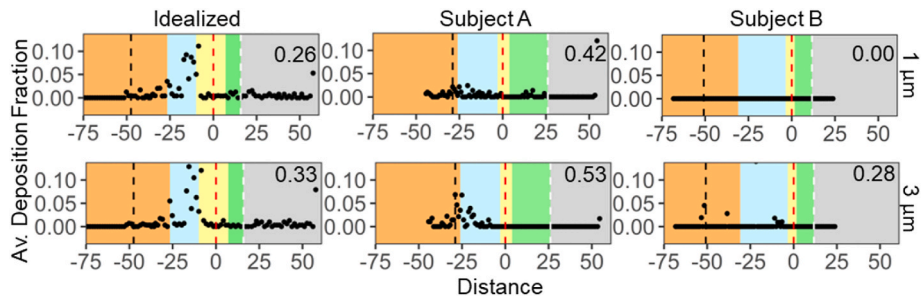


Fig. 6. The average deposition fraction versus the distance along the model centerline for the idealized model (left column), Subject A (middle column), Subject B (right column) for d_p 1 μm (top row) to 3 μm (bottom row). Data shown are for a flow rate of 30 Lpm. The total deposition in the model or UTR is reported in the top right corner of each graph.

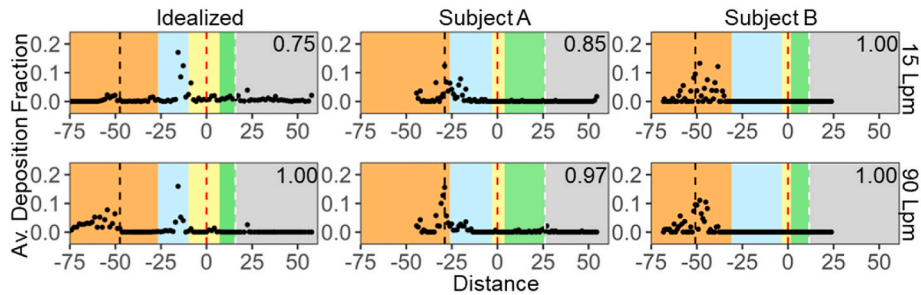


Fig. 7. The average deposition fraction versus the distance along the model centerline for the idealized model (left column), Subject A (middle column), Subject B (right column) for flow rate of 15 Lpm (top row) to 90 Lpm (bottom row). Data shown are for particles of size 10 μm . The total deposition in the model or UTR is reported in the top right corner of each graph.

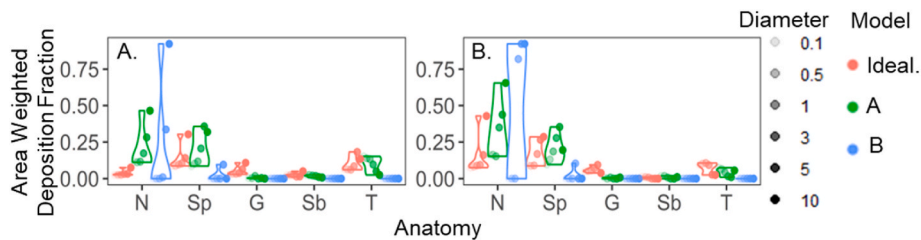


Fig. 8. The anatomical breakdown of the normalized average deposition fraction across the regions of interest; the naso-oropharynx (N), the supraglottis (Sp), the glottis (G), the subglottis (Sb), and the trachea (T) for 15 Lpm (A), and 90 Lpm (B) across particle diameters from 0.1 μm to 10 μm represented by increasing symbol opacity for the idealized model (pink), Subject A (green), and Subject B (blue).

widely varying slopes for the six flow rates represented, but the regression lines consistently overlap each other for each of the flow rates, again supporting that d_p is the more significant factor. This is also visualized by the minimal variation in aerosol deposition between the two breathing extremes shown in Fig. 7. This is somewhat surprising based on a fundamental correlation between aerosol deposition and flow rate [22,47]; however, it is possible that 10 Lpm is already above a critical flow rate in pediatric airways over which there is relatively minimal change in deposition as a function of flow rate. These findings are especially informative for the design of inhaled formulations for pediatric airways, where an insensitivity to flow rate variation may be advantageous following d_p control.

Deposition was next categorized within the UTR by the relevant anatomical features of interest by comparing the area weighted deposition fraction across the naso-oropharynx (N), supraglottis (Sp), glottis (G), subglottis (Sb), and trachea (T) regions. Even when comparing the area weighted deposition fraction, we note that minimal deposition occurs in the glottis and subglottis regions across all three models, while the majority of deposition consistently occurs within naso-oropharynx and supraglottis with some deposition within trachea. Comparing across the three models, statistically significant differences emerge between the anatomical features with peak deposition, as well as the relative deposition ratios between regions. A series of Kruskal-Wallis one-way ANOVAs indicate that differences between models and the anatomy region are significant factors in deposition ($p < 0.00001$ for both parameters), while d_p and flow rate are not significant ($p = 0.1789$ and $p = 0.9817$, respectively). The same is true for robust two-way ANOVAs comparing deposition to model and anatomy ($p < 0.00001$ for both parameters) and comparing to d_p and flow rate ($p = 0.61859$ and 0.89233 , respectively), suggesting that the influence of model and anatomical region of interest are much more significant effectors than diameter and flowrate. However, when comparing all d_p sizes at 15 Lpm to 90 Lpm, overarching trends in peak anatomical regional deposition can be assessed (see Fig. 8).

Comparing regional deposition trends between these two flow rates, we find that increasing the flow rate in the idealized model changes from a peak deposition in supraglottis to an almost equally distributed distribution between naso-oropharynx and supraglottis. Indeed, the idealized model seems to largely under-estimate naso-oropharynx deposition that occurs in the two CT-derived models. Under this same increase in flow rate, Subject A changes from an even distribution of deposition between naso-oropharynx and supraglottis to instead peak deposition in naso-oropharynx, while Subject B retains peak deposition in naso-oropharynx. These trends broadly suggest that the anatomical features with the greatest deposition are increasingly naso-oropharynx as flow rate increases; thus, there is an increase in aerosol deposition in the UTR

upon forced breathing in pediatric subjects. While the idealized model does not well predict these peak anatomical regions or overarching shifting patterns for either Subject A or Subject B, the idealized model basis, the AIT for pediatric subjects, was not originally designed to directly correlate with these sub-anatomic features and yet still manages to well represent overall UTR deposition, especially of Subject A. Interestingly, there are no consistent trends between Subject A and Subject B, indicating that anatomical distribution of aerosol deposition is a potentially unique and personalizable metric of evaluation and characterization, regardless of age “adult”-like or “pediatric”-like features.

Finally, particle deposition within the UTR was plotted as the average deposition fraction as a function of the impaction parameter, d_p^2Q (see Fig. 9). Additionally, the impaction parameter plots were separated by d_p and flow rate. As was expected based on literature, with increasing flow rate and increasing particle d_p , there was a noticeable increase in deposition within the UTR [22,47]. There was more overlap between the idealized model and Subject A, whereas there was less overlap with Subject B. Where overlap does occur, the overall trends are not uniform, as can be seen in the $3 \mu\text{m}$ Fig. 9B panel, where the fraction of deposition is increasing as flow rate increases; however, the range of fraction of deposition that for the idealized model and Subject A spans from 25% to 75% while Subject B spans from nearly 0% to 100%. Thus, even where there is overlap, the overall trend differs between the three models. It is important to note that, as stated previously, the idealized model presented the same trends deposition as a function of d_p and flow rate compared to Subject A and Subject B, while all of the models were statistically significantly different from each other in the anatomical distribution of deposition based on a Kruskal-Wallis one-way ANOVA comparing average deposition fraction to model ($p = 0.019$) as well as a robust two-way ANOVA comparing average deposition fraction to both d_p^2Q and model ($p < 0.00001$ for both parameters, see Supplemental Table S6). These trends were identically shown for another prominent aerosol metric, the Stokes number, shown in Supplemental Methods and Supplemental Fig. S7, supporting the data described for d_p^2Q .

To assess the applicability of this comparison in clinically relevant pharmaceuticals, we set inlet d_p to match an expected distribution of those released from the dry powder inhaler (DPI), Advair® Diskus® according to reported particle spirometry values [20,40,41,43]. Additionally, the inlet velocity was adjusted to reflect a flow rate of 81 Lpm, the required flow rate to activate the Advair® Diskus® [20,43]. While this does not accurately reflect the inhaler apparatus or drug composition of the particles, it does provide a relevant pharmaceutical model of the d_p size distribution and flow rate. The particle distribution MMAD at the inlet was $3.2 \mu\text{m} \pm 1.4 \mu\text{m}$ and, as would be expected based on the previous trends shown for $3 \mu\text{m}$ particles in Fig. 6, there was significant

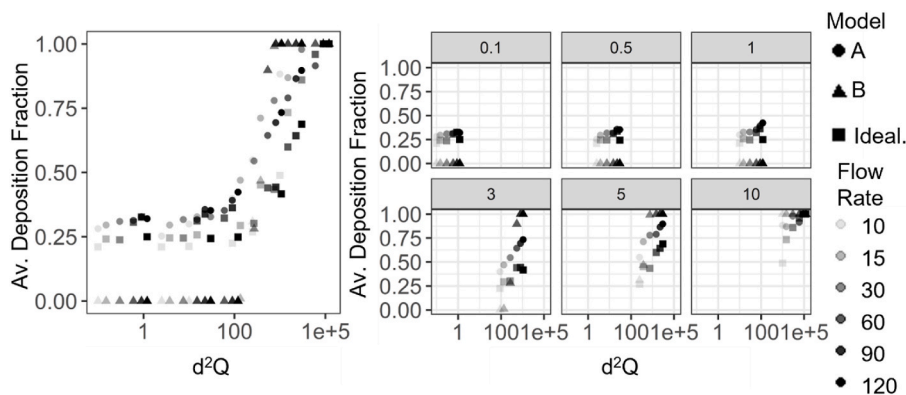


Fig. 9. Fraction of deposition as a function of the impaction parameter, d_p^2Q (left) and the same data separated by particle diameter (each grid represents a particle from 100 nm or 0.1 μm –10 μm) as well as flow rate (visualized as increasing opacity correlates to increasing flow rate from 10 Lpm to 120 Lpm) (right). Subject A is represented by circles (●), Subject B is represented by triangles (▲), and the idealized model is represented by squares (■).

deposition in UTR shown in Fig. 10. Both Subject A and B displayed a significant increase in deposition compared to the idealized model, which underestimated UTR deposition from the expected literature value (see Supplemental Table S4D). Total lung dose (TLD) was determined by the particles that were released from the model and counted at the outlet, which were also analyzed to quantify the MMAD (see Fig. 10). The increased UTR deposition led to decreased TLD for the idealized model. Importantly, the MMAD of Subject B was significantly lower than the reported literature reference, suggesting that the larger particles deposited in the UTR rather than exiting the model and contributing to the TLD.

4. Discussion

This work provides an original characterization of the anatomical and fluid-dynamic features of the upper airways of 6-yr old subjects. Pediatric subject models were developed based on CT scans and compared to an idealized model to assess “pediatric”-like and “adult”-like characteristics of anatomical variables (cricoid ring area shape, narrowing of the glottis versus cricoid ring, and epiglottis angle) and fluid-dynamic variables (turbulent intensity, glottal jet length, and Reynolds number). Classifying these features in this manner is an important step in bridging clinical observations to design of new aerosol therapeutics. We demonstrate aerosol deposition trends that resulted in both overall similarities with key differences of aerosol transport as a function of these developmental anatomical differences. While some aerosol deposition patterns were consistent between the two models, such as statistically significant increases in deposition between $1\ \mu\text{m}$ and $3\ \mu\text{m}$ d_p and less statistically significant increase across flow rates, the impaction parameter, $d_p^2 Q$, revealed stark differences between the two CT-scan models. Most notably, the idealized model better predicted the results of the more “adult”-like model but largely failed to predict behaviors of the more “pediatric”-like model. By identifying the particles depositing in each of the anatomical regions of interest, we further quantified region-specific deposition, finding that the majority of particle deposition occurred in the naso-oropharynx and supraglottis and that the relative deposition in those areas is dependent on both the individual subject and the combination of d_p and flow rate. Using a polydisperse pharmaceutical particle size distribution model based on the Advair® Diskus®, we again find that the idealized model could better predict characteristics of the “adult”-like model, but further differences emerged between all three models. Even in the context of a small sample size, this study provides a critical assessment of the role of developmental pediatric airway features on upper airway deposition, pointing to potential limitations of existing airway approximations and the importance of assessing anatomical features in application of inhaled therapeutics.

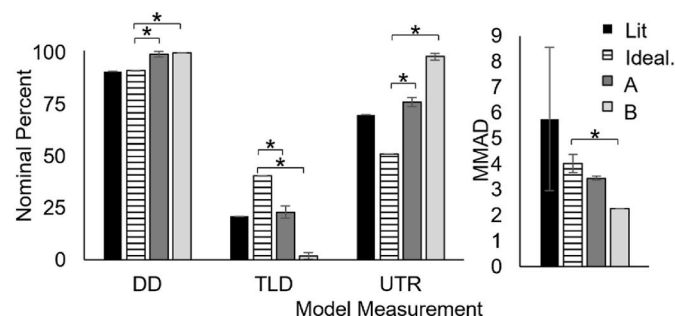


Fig. 10. The nominal percent of particle deposition compared to model measurements of interest (DD: Delivered Dose, TLD: Total Lung Dose, UTR: Upper Throat Region) (left) and the MMAD (right) where error is represented as the standard deviation of the MMAD comparing Literature values [43], the idealized model, Subject A, and Subject B. Statistics are showing T-tests comparing the idealized model to Subject A and Subject B (* $p < 0.05$).

Notably, the use of a common centerline analysis [31] provided a streamlined approach to assess anatomical geometric features and fluid-dynamic metrics to directly quantify whether a model is more “adult”-like or “pediatric”-like for developmental characterization. Comparing two individual scans from 6-year-old subjects using this approach allowed us to directly measure anatomical geometric variations (*i.e.*, cricoid ring area funneling, glottal narrowing, and epiglottis angle) and fluid-dynamic metrics (*i.e.*, turbulence intensity, glottal jet length, and recirculation velocity ratios). The centerline analysis approach allowed for facile normalization and alignment of these unique geometries and direct inter-patient assessments, applicable for future evaluations of inter-patient differences across a wide range of airway geometries. Moreover, our approach sets up an important framework to streamline the characterization of these anatomical geometric and fluid-dynamic features within pediatric development directly from CT scans, allowing us to assess the resultant aerosol deposition implications and apply this system to evaluate key metrics for pharmaceutical design and clinical applications.

The two CT scan-based models were both of 6-year-old healthy subjects; however, it is clear that developmental differences between the two subjects resulted in geometric differences in their anatomies. As previously discussed, the age of 6 is a dynamic time for airway maturation. Many 6-year-old children will have started to develop “adult”-like characteristics, but there is always a range of what is normal development [3,4,8]. While we only have a limited sample of two individuals, our models demonstrate that not all features develop simultaneously. For instance, in Subject B the larynx is descending and moving more posterior, meaning that the angle is progressing toward the acute angle of the adult, while still remaining quantifiably in the “pediatric”-like definition. Subject B has a funnel-shaped cricoid ring area, a narrower cricoid ring area than the glottis, and a somewhat obtuse epiglottis angle, all of which are “pediatric”-like features. However, the glottis is narrower than the cricoid ring and the epiglottis is obtusely angled, which are “adult”-like features. To summarize, model Subject A displays a mixture of “adult”-like and “pediatric”-like features that are predominantly “adult”-like while model Subject B displays predominantly “pediatric”-like features. While there are a range of “pediatric”-like and “adult”-like upper airway characteristics in these two models, these represent a very restrictive data set and further work is needed to evaluate how representative these geometries are of the overall 6-year-old population. It is important to note that these two models represent one male and one female subject. Patient sex plays a significant role in upper airway anatomical development in pubescent pediatric subjects, such as the length of the trachea; however, the descending larynx and the cricoid ring developing a wider and more cylindrical shape is not statistically significantly different amongst male and female pediatric subjects [3,51,52]. Thus, the female subject features resulting in a more “adult”-like throat compared to the male subject features are not expected to be indicative of sex-based developmental progression. This mixture of features is also represented in the fluid dynamic metrics; the low turbulence intensity, long glottal jet, and low Reynolds number in Subject A are all “adult”-like characteristics. However, Subject B had a high turbulence intensity and short glottal jet, which are “pediatric”-like features, and a low Reynolds number, resulting in a mixture of predominantly “pediatric”-like features. Additionally, it can be seen in Figs. 3 and 4 that the recirculation is lower in an “adult”-like model compared to a “pediatric”-like model by the visibly negligible changes in axial and tangential velocity (Fig. 4) as well as a relatively low ratio between the two (Fig. 3). It has previously been shown in literature that pediatric subjects at 5 years old and 10 years old have shorter glottal jets, more intense recirculations with higher axial velocities, and higher overall relative recirculations compared to their adult counterparts [12,50]. To summarize between the anatomical and fluid-dynamic metrics, Subject A has a predominantly “adult”-like upper airway while Subject B has a predominantly

“pediatric”-like upper airway, though they both have a mixture of features that is likely characteristic of this developmental age range. Additional samples are needed to fully characterize the dynamic range of inter-patient variability occurring between patients in this period of rapid development to ultimately deconvolute the role of sex and age on specific aerosol deposition effects, which will be pursued in follow-on studies.

The anatomical and fluid-dynamic variations between Subject A and Subject B were shown to influence the resultant aerosol deposition patterns. There were some patterns for which there was consistency, such as the statistically significant difference in deposition between particles that were 1 μm and 3 μm in diameter. There was also consistently less statistically significant difference in deposition patterns as flow rate was varied. This importance of d_p compared to flowrate and a d_p that is higher than 1 μm indicates that a pharmaceutical aerosol designed for adult lungs centered around a peak lung delivery of 1 μm could be too large for pediatric subjects regardless of their developmental state and breathing profile [47]. However, the impaction parameter $d_p^2 Q$, was shown to have starkly different patterns when comparing Subject A to Subject B, such that Subject A had low deposition which gradually increased with increasing $d_p^2 Q$ while Subject B had no deposition that sharply increased with increasing $d_p^2 Q$. Subject A is more “adult”-like and was expected to have less deposition than Subject B, but instead frequently showed more deposition than Subject B. We hypothesize possible causes of this observation; namely fluid-dynamic differences and intersubject variability. The fluid-dynamic recirculations and turbulence are more prominent in Subject B and might result in flow patterns that reduce particle deposition; for example, if a recirculation was driving particles away from a site that would otherwise have high deposition, then the deposition might decrease. Alternatively, it is possible that this is subject-specific and due to inherent intersubject variability. We have concluded that to determine the influence of fluid-dynamic or intersubject variability on the resultant $d_p^2 Q$ trend would require higher sample sizes. Finally, the anatomical regions where deposition occurred most frequently was the naso-oropharynx and the supraglottis for both Subject A and B, although deposition in these regions was consistently larger for Subject B. The characteristic regional deposition was statistically significantly different between all models, suggesting that these specific anatomical UTR regions are independent of development and personalizable. It is notable that only two subjects were compared and this study would benefit from including more models to assess any potential outliers, though this was partially addressed through the use of the idealized model, which is intended to capture a broad range of relevant features.

Development of inhaled therapeutics for pediatric subjects relies on use of various preclinical models to understand air and aerosol flows through the upper airways; use of effective models is especially important for pediatric patients due to ethical and logistical challenges of expansive clinical studies [53,54]. High-throughput pharmaceutical studies aimed at pediatric patient treatments often utilize *in vitro* idealized models of the upper airways, such as the AIT for pediatric subjects which was the basis for the RDD idealized model used in this work [22,44]. The AIT for pediatric subjects was designed based on the adult version and scaled by a factor of 0.62 to mimic *in vitro* data from models of subjects 6–14 years old [22,55]. Idealized pediatric throat models are critical for integrating pediatric specifications for aerosol design into the pharmaceutical industry in a concise and consistent manner and have supported shift in manufacturing practices to focus on pediatric needs. However, the transition from a “pediatric” throat to an “adult” throat can still be in progress at 6 years of age, which is the lower end of manufacturer’s suggested for the pediatric AIT. Our results demonstrate that scaling the AIT may fail to consider important geometric considerations that occur in 6-year-olds. The idealized model used in this work has a cylindrical shaped cricoid ring area, a narrower glottis than the cricoid ring, and the most acute epiglottis of all of the models, all of which are “adult”-like features (see Fig. 2 and Table 1) and

which influence local fluid features. These fluid-dynamic features for the idealized model were categorized as “adult”-like features, namely the low turbulence intensity, long glottal jet, and low Reynolds number through the model (see Figs. 3–5 and Table 2). The hypothesis that this model would better predict a more “adult”-like anatomical geometry was supported by overlapping trends for the impaction parameter, $d_p^2 Q$, and the pharmaceutical particle size distribution model deposition for the idealized model and Subject A, the CT scan model with the more “adult”-like features (see Figs. 9 and 10). There were also some trends which were consistent amongst all models, such as the statistically significant increase in deposition between particle diameters of 1 and 3 μm and the less significant differences of increasing flow rate on particle deposition (see Figs. 5–7). There was a trend independent of “adult”-like or “pediatric”-like features that seemed to be subject specific; all models had variation in peak particle deposition between the anatomical features. There were more particles depositing in the naso-oropharynx and supraglottis but the feature with peak anatomical deposition was independent of d_p and flow rate (see Fig. 8). While the idealized model did not predict the deposition of the CT scan models, it did mirror the independent intersubject variability. Key parameters in pharmaceutical and clinical aerosol research, such as the critical size in d_p , consistent trends with flow rate, and independent peak anatomical deposition may be predicted or mirrored by the idealized model consistently across individual subjects, but we have demonstrated that there are metrics, such as $d_p^2 Q$ and MMAD, that an idealized model based on the AIT is better suited to predict for a subject with a more “adult”-like upper airway than a more “pediatric”-like upper airway.

To evaluate these models on a relevant therapeutic, we approximated the particle size distribution present in the Advair® Diskus® and assessed the upper airway deposition. The Advair® Diskus® has been one of the most commonly prescribed medication for asthma, the most common chronic illness in pediatric patients in the United States [56–58]. The idealized model aligned with literature was closer in comparison to Subject A, especially in the MMAD where there was no statistically significant difference, compared to Subject B. Additionally, the MMAD of Subject B was shown to be lower, suggesting that there is more upper airway deposition for the more “pediatric”-like model. Additionally, it was shown that naso-oropharynx and supraglottis deposition increased as flow rate increased, suggesting that there is more delivery to these upper airway regions upon a forced breath such as is required during inhaler use. It is well known that high off-target naso-oropharynx deposition is an issue in asthma medication for pediatric patients [42]. Additionally, it has been shown that pediatric subjects exhibit increased deposition in the lower airways compared to adult subjects and that this leads to inaccurate dosing for pediatric subjects; the intersubject variability observed here may influence the resultant lower airway deposition and necessitates consideration of upper airways in predicting lower airway deposition and dose disparities [59]. It is important to note that the correlation between anatomy and predicted inhaler function is based on a CT scans which are not always available or practical. Also, this work indicates anatomy influences correlation to idealized models; however, it is impossible to fully know a subject’s anatomy without a CT scan, and thus the appropriate corresponding model is not identifiable. Thus, remaining work would be necessary to translate this work to a clinical setting and implement guidelines based on these results. These data suggest that, while idealized models based on the AIT are representative of some pediatric patients, there are patients who fall in the age range of those represented by idealized approximations and do not present the same deposition trends. Additionally, while this pharmaceutical model is only representative of the size distribution of the Advair® Diskus®, it obviates the need to assess pediatric airways separately from adult airways in pharmaceutical design and presents a framework to accomplish this representation.

While this work brings the field of pediatric aerosols one step closer to understanding and utilizing fundamental aspects of airway

development and resultant aerosol phenomenon, there exist several limitations that remain to be addressed. Importantly, the glottises of these CFPD models are static, while *in vivo*, vocal cords adduct (come together) in loose fashion during expiration and close tightly during phonation and swallowing [3,4,8]. On inspiration they abduct (move apart) to maximize air intake. The utilization of CT scans collected from real patients imposes constraints on image collection, namely the breathing profile and mouth position were not controlled, and since a CT scan is a snapshot in time it is possible to catch a patient during expiration or with a closed mouth [8]. We may be seeing this in play with Subject A as the angle and shape of the airway is consistent with pediatric anatomy, but the glottis is uncharacteristically narrow for an airway that still has a funnel-shape. Additionally, the oral cavity is notably smaller than those used to create idealized airway models. Alternative methods for airway modeling may provide complementary information, with methods such as cadaver casts or MR and video-bronchoscope imaging yielding different airway measures that can provide additional insight into resultant deposition patterns [3,4,8]. Our CFPD analysis was performed on a static framework at a fixed inhalation flow rate, whereas a real patient would experience variable flow rates encompassing exhalation; additional studies capable of capturing these critical dynamics would further increase the physiological relevance of this work [60]. Additionally, particles were modeled in a dilute phase and may behave differently due to particle-particle interactions and coagulation that can occur in pharmaceuticals, which may have been an especially impactful limitation in the Advair® Diskus® model [44,61]. In this case, our model is intended to generally evaluate broad trends in similar DPI products, such as the Wixela Inhub which was designed based on the Advair® Diskus® [62,63] but may not be representative of significantly different systems such as liquid nebulizer formulations. Finally, the data produced here are not intended to function as an immediately implementable guideline in clinical applications and requires future work to achieve such practicality. Recent studies including dense particulate phase modeling of DPIs indicate that the overall deposition in the UTR would be expected to increase, although we would anticipate similar overall patterns of deposition [64, 65].

This study highlights significant inter-patient variability at this key stage of childhood development and points to a need to further understand these anatomical variations to optimize aerosol therapeutics. Follow-on work should address how to incorporate variations in pediatric airway aerosol requirements into pharmaceutical and clinical settings. Methodical assessment of subpopulations represented by varying degrees of anatomical development would provide clarity toward the implementation of such guidelines or requirements. The overestimation of delivery to the lungs predicted by the more “pediatric”-like lung in the pharmaceutical approximation and the low deposition at small particle diameters exemplifies the need to pursue personalized therapeutics for pediatric patients instead of prescribing therapeutics intended for adults or off-label formulations, as is commonly done for pediatric patients. Additionally, the limited deposition regions to the uppermost anatomical features insinuates that targeting deposition to the glottis, subglottis, and trachea would be difficult; this has important implications for development of therapeutics for diseases which impact these specific airway features. Overall, we envision future work will build on this quantitative pediatric inter-patient evaluation to ultimately improve our understanding of airway development in pediatric patients and lead to improved pharmaceutical interventions.

Declaration of competing interest

The authors declare no conflict of interest.

Acknowledgements

Research reported in this publication was supported by the National

Institute of General Medical Sciences of the National Institutes of Health under award number R35GM142866A (CAF). Emily Kolewe was supported by the National Institute of Heart, Lung, and Blood Institute of the National Institutes of Health under award number F31HL160153. The content is solely the responsibility of the authors and does not necessarily represent the official views of the National Institutes of Health.

Appendix A. Supplementary data

Supplementary data to this article can be found online at <https://doi.org/10.1016/j.compbimed.2022.106058>.

References

- [1] B. Devlin, Pharynx and Larynx, *Histopathology Specimens: Clinical, Pathological and Laboratory Aspects*, 2017, p. 179.
- [2] K. Ahooshosh, O. Pourmehran, H. Aminfar, M. Mohammadpourfard, M. Sarafraz, H. Hamishehkar, Development of human respiratory airway models: a review, *Eur. J. Pharmaceut. Sci.* 145 (2020), 105233.
- [3] P.G. Dalal, D. Murray, A.H. Messner, A. Feng, J. McAllister, D. Molter, Pediatric laryngeal dimensions: an age-based analysis, *Anesth. Analg.* 108 (2009) 1475–1479.
- [4] M. Di Cicco, A. Kantar, B. Masini, G. Nuzzi, V. Ragazzo, D. Peroni, Structural and functional development in airways throughout childhood: children are not small adults, *Pediatr. Pulmonol.* 56 (2021) 240–251.
- [5] C.-L. Lin, M.H. Tawhai, G. McLennan, E.A. Hoffman, Characteristics of the turbulent laryngeal jet and its effect on airflow in the human intra-thoracic airways, *Respir. Physiol. Neurobiol.* 157 (2007) 295–309.
- [6] J.E. Eckenhoff, Some Anatomic Considerations of the Infant Larynx Influencing Endotracheal Anesthesia, *The Journal of the American Society of Anesthesiologists*, The American Society of Anesthesiologists, 1951, pp. 401–410.
- [7] R. Bayeux, Tubage du larynx dans le croup, *Presse Med.* 20 (1897) 1–4.
- [8] J.-H. Kwon, Y.H. Shin, N.-S. Gil, H. Yeo, J.S. Jeong, Analysis of the functionally-narrowest portion of the pediatric upper airway in sedated children, *Medicine* (2018) 97.
- [9] R.S. Litman, E.E. Weissend, D. Shibata, P.-L. Westesson, Developmental changes of laryngeal dimensions in unparalyzed, sedated children, *The Journal of the American Society of Anesthesiologists* 98 (2003) 41–45.
- [10] T.E. Corcoran, N. Chigier, Characterization of the laryngeal jet using phase Doppler interferometry, *J. Aerosol Med.* 13 (2000) 125–137.
- [11] Q. Deng, C. Ou, J. Chen, Y. Xiang, Particle deposition in tracheobronchial airways of an infant, child and adult, *Sci. Total Environ.* 612 (2018) 339–346.
- [12] P. Das, E. Nof, I. Amirav, S.C. Kassinos, J. Sznitman, Targeting inhaled aerosol delivery to upper airways in children: insight from computational fluid dynamics (CFD), *PLoS One* (2018) 13.
- [13] B. Asgharian, M. Menache, F. Miller, Modeling age-related particle deposition in humans, *J. Aerosol Med.* 17 (2004) 213–224.
- [14] I. Amirav, M.T. Newhouse, Deposition of small particles in the developing lung, *Paediatr. Respir. Rev.* 13 (2012) 73–78.
- [15] G. Xu, C. Yu, Effects of age on deposition of inhaled aerosols in the human lung, *Aerosol. Sci. Technol.* 5 (1986) 349–357.
- [16] J.M. Oakes, S.C. Roth, S.C. Shadden, Airflow simulations in infant, child, and adult pulmonary conducting airways, *Ann. Biomed. Eng.* 46 (2018) 498–512.
- [17] P.W. Longest, S. Vinchurkar, T. Martonen, Transport and deposition of respiratory aerosols in models of childhood asthma, *J. Aerosol Sci.* 37 (2006) 1234–1257.
- [18] J.T. Katan, P. Hofemeier, J. Sznitman, Computational models of inhalation therapy in early childhood: therapeutic aerosols in the developing acinus, *J. Aerosol Med. Pulm. Drug Deliv.* 29 (2016) 288–298.
- [19] L. Agertoft, S. Pedersen, K. Nikander, Drug delivery from the Turbuhaler and Nebuhaler pressurized metered dose inhaler to various age groups of children with asthma, *J. Aerosol Med.* 12 (1999) 161–169.
- [20] J. Weers, A. Clark, The impact of inspiratory flow rate on drug delivery to the lungs with dry powder inhalers, *Pharmaceut. Res.* 34 (2017) 507–528.
- [21] W. Vincken, M.L. Levy, J. Scullion, O.S. Usmani, P.R. Dekhuijzen, C.J. Corrigan, Spacer devices for inhaled therapy: why use them, and how? *ERJ open research* (2018) 4.
- [22] L. Golshahi, W. Finlay, An idealized child throat that mimics average pediatric oropharyngeal deposition, *Aerosol. Sci. Technol.* 46 (2012) i–iv.
- [23] A.A. Borojeni, M.L. Noga, A.R. Martin, W.H. Finlay, An idealized branching airway geometry that mimics average aerosol deposition in pediatric central conducting airways, *J. Aerosol Sci.* 85 (2015) 10–16.
- [24] Y. Zhang, W.H. Finlay, Measurement of the effect of cartilaginous rings on particle deposition in a proximal lung bifurcation model, *Aerosol. Sci. Technol.* 39 (2005) 394–399.
- [25] A.A. Borojeni, G.J. Garcia, M.G. Moghaddam, D.O. Frank-Ito, J.S. Kimbell, P. W. Laud, L.J. Koenig, J.S. Rhee, Normative ranges of nasal airflow variables in healthy adults, *Int. J. Comput. Assist. Radiol. Surg.* 15 (2020) 87–98.
- [26] H. Wachtel, D. Bickmann, J. Breitzkreutz, P. Langguth, Can Pediatric Throat Models and Air Flow Profiles Improve Our Dose Finding Strategy, *Respiratory Drug Delivery*, Davis Healthcare International River Grove, Illinois, 2010, pp. 195–204.
- [27] W. Mokhtar, C. Spore, B. Upreti, S. Boer, Model Development for Numerical Simulation of Aortic Blood Flow, 2019.

- [28] J. Holzki, K.A. Brown, R.G. Carroll, C.J. Cote, The anatomy of the pediatric airway: has our knowledge changed in 120 years? A review of historic and recent investigations of the anatomy of the pediatric larynx, *Pediatric Anesthesia* 28 (2018) 13–22.
- [29] A.A.o.O. Surgeons, A.C.o.E. Physicians, *Critical Care Transport*, Jones & Bartlett Learning 2009.
- [30] L. Antiga, M. Piccinelli, L. Botti, B. Ene-Iordache, A. Remuzzi, D.A. Steinman, An image-based modeling framework for patient-specific computational hemodynamics, *Med. Biol. Eng. Comput.* 46 (2008) 1097–1112.
- [31] A. Kuprat, M. Jalali, T. Jan, R. Corley, B. Asgharian, O. Price, R. Singh, S. Colby, C. Darquenne, Efficient bi-directional coupling of 3D computational fluid-particle dynamics and 1D multiple path particle dosimetry lung models for multiscale modeling of aerosol dosimetry, *J. Aerosol Sci.* 151 (2021), 105647.
- [32] Y. Feng, J. Zhao, X. Chen, J. Lin, An in silico subject-variability study of upper airway morphological influence on the airflow regime in a tracheobronchial tree, *Bioengineering* 4 (2017) 90.
- [33] Y. Ostrovski, S. Dorfman, M. Mezhericher, S. Kassinos, J. Sznitman, Targeted Drug Delivery to Upper Airways Using a Pulsed Aerosol Bolus and Inhaled Volume Tracking Method, Flow, Turbulence and Combustion, 2018.
- [34] X. Chen, Y. Feng, W. Zhong, C. Kleinstreuer, Numerical investigation of the interaction, transport and deposition of multicomponent droplets in a simple mouth-throat model, *J. Aerosol Sci.* 105 (2017) 108–127.
- [35] J. Kim, P. Moin, R. Moser, Turbulence statistics in fully developed channel flow at low Reynolds number, *J. Fluid Mech.* 177 (1987) 133–166.
- [36] A. Gosman, E. Loannides, Aspects of computer simulation of liquid-fueled combustors, *J. Energy* 7 (1983) 482–490.
- [37] Y. Wang, P. James, On the effect of anisotropy on the turbulent dispersion and deposition of small particles, *Int. J. Multiphas. Flow* 25 (1999) 551–558.
- [38] E.L. Kolewe, Y. Feng, C.A. Fromen, Realizing lobe-specific aerosol targeting in a 3D-printed in vitro lung model, *J. Aerosol Med. Pulm. Drug Deliv.* 34 (1) (2020) 42–56.
- [39] M. Ali, Effects of Three Dry Powder Inhalers on Deposition of Aerosolized Medicine in the Human Oral-Pharyngeal-Laryngeal Regions, 2015.
- [40] M. Ali, R.N. Reddy, M.K. Mazumder, Simultaneous characterization of aerodynamic size and electrostatic charge distributions of inhaled dry powder inhaler aerosols, *Curr. Respir. Med. Rev.* 4 (2008) 2–5.
- [41] M.W. Jetzer, B.D. Morrical, D.P. Ferguson, G. Imanidis, Particle interactions of fluticasone propionate and salmeterol xinafoate detected with single particle aerosol mass spectrometry (SPAMS), *Int. J. Pharm.* 532 (2017) 218–228.
- [42] J.G. Weers, Y.-J. Son, M. Glusker, A. Haynes, D. Huang, N. Kadrichu, J. Le, X. Li, R. Malcolmson, D.P. Miller, Idealhalers versus realhalers: is it possible to bypass deposition in the upper respiratory tract? *J. Aerosol Med. Pulm. Drug Deliv.* 32 (2019) 55–69.
- [43] K.T. Ung, Design of Inhaled Insulin Dry Powder Formulations to Bypass Deposition in the Human Extrathoracic Region and Enhance Lung Targeting, 2016.
- [44] L. Crispps, J. Paul, Pharmaceutical Aerosol Formulation of Salmeterol and Fluticasone Propionate, Google Patents, 2003.
- [45] M. Gharahgouzlou, V. Khajooe, M. Moein, M. Rezvani, Peak Expiratory Flow Rate in Healthy Children from Tehran, 2003.
- [46] M.H. Bentsen, M. Eriksen, M.S. Olsen, T. Markestad, T. Halvorsen, Electromagnetic Inductance Plethysmography Is Well Suited to Measure Tidal Breathing in Infants, vol. 2, ERJ open research, 2016.
- [47] J.S. Patton, P.R. Byron, Inhaling medicines: delivering drugs to the body through the lungs, *Nat. Rev. Drug Discov.* 6 (2007) 67–74.
- [48] V.A. Marple, D.L. Roberts, F.J. Romay, N.C. Miller, K.G. Truman, M. Van Oort, B. Olsson, M.J. Holroyd, J.P. Mitchell, D. Hochrainer, Next generation pharmaceutical impactor (A new impactor for pharmaceutical inhaler testing). Part I: design, *J. Aerosol Med.* 16 (2003) 283–299.
- [49] A. Haghnegahdar, Y. Feng, X. Chen, J. Lin, Computational analysis of deposition and translocation of inhaled nicotine and acrolein in the human body with e-cigarette puffing topographies, *Aerosol. Sci. Technol.* 52 (2018) 483–493.
- [50] J. Xi, X. Si, J.W. Kim, A. Berlinski, Simulation of airflow and aerosol deposition in the nasal cavity of a 5-year-old child, *J. Aerosol Sci.* 42 (2011) 156–173.
- [51] O. Ronen, A. Malhotra, G. Pillar, Influence of gender and age on upper-airway length during development, *Pediatrics* 120 (2007) e1028–e1034.
- [52] Ö. Incebay, A. Köse, F.E. Aydınli, E. Özcebe, The effects of age and gender on laryngeal aerodynamics in the children population, *J. Voice* 34 (2020) 300–300. e346, e327.
- [53] D.N. Price, N.K. Kunda, P. Muttli, Challenges associated with the pulmonary delivery of therapeutic dry powders for preclinical testing, *KONA Powder and Particle Journal* 36 (2019) 129–144.
- [54] S. Ehrmann, O. Schmid, C. Darquenne, B. Rothen-Rutishauser, J. Sznitman, L. Yang, H. Barosova, L. Vecellio, J. Mitchell, N. Heuze-Vourc'h, Innovative preclinical models for pulmonary drug delivery research, *Exp. Opin. Drug Deliv.* 17 (2020) 463–478.
- [55] K.W. Stapleton, E. Guentsch, M. Hoskinson, W.H. Finlay, On the suitability of k-ε turbulence modeling for aerosol deposition in the mouth and throat: a comparison with experiment, *J. Aerosol Sci.* 31 (2000) 739–749.
- [56] H.S. Zahran, C.M. Bailey, S.A. Damon, P.L. Garbe, P.N. Breyse, Vital signs: asthma in children—United States, 2001–2016, *MMWR (Morb. Mortal. Wkly. Rep.)* 67 (2018) 149.
- [57] H.J. Zar, T.W. Ferkol, The Global Burden of Respiratory Disease—Impact on Child Health, Wiley Online Library, 2014, pp. 430–434.
- [58] D. Cipolla, I. Gonda, L. Respidex, PUBLIC INTEREST & INCENTIVES FOR INNOVATORS OF INHALED PRODUCTS.
- [59] K. Poorbahrani, I.E. Vignon-Clementel, S.C. Shadden, J.M. Oakes, A whole lung in silico model to estimate age dependent particle dosimetry, *Sci. Rep.* 11 (2021) 1–12.
- [60] J. Zhao, Y. Feng, C.A. Fromen, Glottis motion effects on the particle transport and deposition in a subject-specific mouth-to-trachea model: a CFPD study, *Comput. Biol. Med.* 116 (2020), 103532.
- [61] J. Tu, K. Inthavong, G. Ahmadi, Computational fluid and particle dynamics (CFPD): an introduction, computational fluid and particle dynamics in the human respiratory system, Springer (2013) 1–18.
- [62] A. Cooper, J. Parker, M. Berry, R. Wallace, J. Ward, R. Allan, Wixela Inhub: dosing performance in vitro and inhaled flow rates in healthy subjects and patients compared with Advair Diskus, *J. Aerosol Med. Pulm. Drug Deliv.* 33 (2020) 323–341.
- [63] D. Ng, E.M. Kerwin, M.V. White, S.D. Miller, S. Haughie, J.K. Ward, R. Allan, Clinical bioequivalence of Wixela Inhub and Advair Diskus in adults with asthma, *J. Aerosol Med. Pulm. Drug Deliv.* 33 (2019) 99–107.
- [64] Y. Feng, J. Zhao, H. Hayati, T. Sperry, H. Yi, Tutorial: understanding the transport, deposition, and translocation of particles in human respiratory systems using Computational Fluid-Particle Dynamics and Physiologically Based Toxicokinetic models, *J. Aerosol Sci.* 151 (2021), 105672.
- [65] J. Zhao, A. Haghnegahdar, Y. Feng, A. Patil, N. Kulkarni, G.J.P. Singh, G. Malhotra, R. Bharadwaj, Prediction of the carrier shape effect on particle transport, interaction and deposition in two dry powder inhalers and a mouth-to-G13 human respiratory system: a CFD-DEM study, *J. Aerosol Sci.* 160 (2022), 105899.